TU Delft

Delft University of Technology

Spatially-graded 3D-printed viscoelastic truss metamaterials for impact trajectory control and energy absorption

Radi, Kaoutar; Glaesener, Raphaël N.; Kumar, Siddhant; Kochmann, Dennis M.

DOI
10.1016/j.taml.2024.100553

Publication date
2024

Document Version
Final published version

Published in
Theoretical and Applied Mechanics Letters

Citation (APA)
Radi, K., Glaesener, R. N., Kumar, S., & Kochmann, D. M. (2024). Spatially-graded 3D-printed viscoelastic truss metamaterials for impact trajectory control and energy absorption. *Theoretical and Applied Mechanics Letters*, *14*(5), Article 100553. https://doi.org/10.1016/j.taml.2024.100553

Important note
To cite this publication, please use the final published version (if applicable).
Please check the document version above.

Copyright
Other than for strictly personal use, it is not permitted to download, forward or distribute the text or part of it, without the consent of the author(s) and/or copyright holder(s), unless the work is under an open content license such as Creative Commons.

Takedown policy
Please contact us and provide details if you believe this document breaches copyrights.
We will remove access to the work immediately and investigate your claim.

This work is downloaded from Delft University of Technology.
For technical reasons the number of authors shown on this cover page is limited to a maximum of 10.

Theoretical and Applied Mechanics Letters 14 (2024) 100553

Contents lists available at ScienceDirect

Theoretical and Applied Mechanics Letters

journal homepage: www.elsevier.com/locate/taml

Spatially-graded 3D-printed viscoelastic truss metamaterials for impact trajectory control and energy absorption

Kaoutar Radi[a], Raphaël N. Glaesener[a], Siddhant Kumar[b], Dennis M. Kochmann[a,*]

[a] Mechanics & Materials Lab, Department of Mechanical and Process Engineering, ETH Zürich 8092, Switzerland
[b] Mechanics & Materials Computing Lab, Department of Materials Science & Engineering, TU Delft 2628 CN, Netherlands

ARTICLE INFO

Keywords:
Metamaterial
3D Printing
Viscoelasticity
Impact
Truss
Finite element method

ABSTRACT

This study demonstrates that two- and three-dimensional spatially graded, truss-based polymeric-material metamaterials can be designed for beneficial impact mitigation and energy absorption capabilities. Through a combination of numerical and experimental techniques, we highlight the broad property space of periodic viscoelastic trusses, realized using 3D printing via selective laser sintering. Extending beyond periodic designs, we investigate the impact response of spatially variant viscoelastic lattices in both two and three dimensions. Our result reveal that introducing spatial variations in lattice topology allows for redirecting of the impact trajectory, opening new opportunities for engineering and tailoring lightweight materials with target impact functionality. This is achieved through the combined selection of base material and metamaterial design.

1. Introduction

While research on truss-based metamaterials has largely focused on periodic assemblies of structural members, spatial variations in the structural architecture expand the design space and admit locally optimized, location-dependent mechanical properties. Examples include orthopedic implants [1,2], the soles of running shoes [3], and soft robots [4], which all benefit from architected materials with a non-periodic architecture or heterogeneous material distribution. In addition to optimizing the local effective, macroscale mechanical behavior (including extreme cases such as negative compressibility [5] or Poisson effect [6]), spatial variation in the architectural design can facilitate new functionality. Such concepts have been explored at large scales, e.g., in the design of space solar sails [7] and deployable solar arrays [8]. Combining different types of multistable unit cells at smaller scales in a spatial tessellation [9] has enabled mechanical logic and reconfigurability. In contrast, the functional grading between soft and stiff 3D-printed structural components or regions has enabled pre-programmed motion through mechanisms [10] and enhanced the performance of soft robots [11]. Note that in this study we refer to 'metamaterials' as a synonym for 'architected materials', as is often customary in the metamaterials community – not necessarily implying that none of the reported material properties cannot be found in nature but rather highlighting that the structural architecture controls the material properties, which may indeed lie outside the range of natural materials.

Additively manufactured metamaterials are often polymeric and viscoelastic; i.e., the base material dissipates energy and renders the mechanical response time- and history-dependent. What is disadvantageous for wave guidance in acoustic metamaterials [12] can be beneficial for energy absorption applications [3,13,14]. The viscoelastic relaxation, creep, and time-dependent response have promoted new effects and applications [15] ranging from viscoelastic snapping [15], rate-dependent buckling patterns and bistable beams [16,17] to advanced and tailored vibration damping [18,19] and frequency control and dispersion tuning in soft phononic crystals [20].

Impact into a metamaterial by a stiff object is a particular scenario that is of practical relevance (e.g., for shoe soles, protective bumpers, planetary landers, and packaging) and leverages the energy absorption capability. Importantly, the impact behavior depends on the structural architecture and the base material and has been investigated across scales. Both large-scale [14] and small-scale [21] truss lattices can absorb significant impact energy, spread the impact load in time and space, and reduce the peak impact stress—depending on the truss topology. In those studies, the metallic base materials led to significant plastic deformation and permanent crushing. Brittle carbon-based nanolattices [22], by contrast, were shown to absorb energy during impact through dynamic resonance and failure mechanisms, depending on the impact speed and lattice design.

Low-density polymer-based truss lattices have significant damping, so that dynamic (inertial) effects are often negligible. In contrast, the

* Corresponding author.
E-mail address: dmk@ethz.ch (D.M. Kochmann).
URL: http://www.mm.ethz.ch (D.M. Kochmann)

https://doi.org/10.1016/j.taml.2024.100553
Received 12 January 2024; Received in revised form 19 August 2024; Accepted 29 August 2024
Available online 24 September 2024
2095-0349/© 2024 The Author(s). Published by Elsevier Ltd on behalf of The Chinese Society of Theoretical and Applied Mechanics. This is an open access article under the CC BY license (http://creativecommons.org/licenses/by/4.0/)

deformation behavior shows significant rate dependence due to the viscoelasticity of the base material [23]. A good body of prior work has focused on the linear elastic static and dynamic effective response of truss lattices, their large-deformation nonlinear elastic buckling behavior, their impact absorption focusing on stiff materials, and the effective viscoelastic quasistatic behavior. Yet, the overall available design space of periodic and significantly spatially graded viscoelastic truss-based metamaterials has remained unexplored. To this end, we discuss the performance of periodic and graded trusses in three and two dimensions (3D and 2D, respectively), focusing on shedding light on untapped opportunities in their design and property spaces.

2. Stiffness versus energy absorption

Materials' stiffness and energy-absorbing capabilities are classically inversely related [24]. Stiff materials like metals and ceramics typically show low energy absorption and fail under significant loads. By contrast, soft materials such as polymers, rubbers, and foams generally are excellent energy absorbers but exhibit low stiffness. Metamaterials have overcome this classical distinction since their base material and architecture can be tailored independently—allowing for resilient and compliant truss [25] or shell networks [26] made of stiff ceramic base materials. While the effective stiffness is a well-defined linear and average property of a structure [27] (which can be determined by homogenizing a single unit cell in case of periodic designs), the energy absorption upon impact is less trivial to predict and involves the overall structural response. Depending on the impact regime, it may involve large deformation, buckling, crushing, and localization [28] and lead to anything from full recovery to full destruction of the structure [21,22].

Truss lattices are appealing not only for their tunable mechanical properties but also for their low mass density, reaching exceptionally high stiffness- and strength-to-weight ratios [29–31], owing to their low relative density, or fill fraction, $\bar{\rho}$. The influence of density (to leading order) is often summarized in scaling laws [32–34], e.g., for Young's modulus E of the type $E \propto \rho^{\alpha}$, where exponent $\alpha \geq 1$ depends on the truss topology (the lower bound stemming from the Voigt upper bound, and $\alpha = 2$ and 4 being characteristic for, respectively, stretching- and bending-dominated cellular architectures). Regarding impact energy absorption, the low relative density of truss lattices promotes considerably nonlinear deformation, buckling, and—ultimately—contact between beams, which serve as excellent dissipation mechanisms. However, the relationship between density, stiffness, and energy absorption is nontrivial as illustrated in Fig. 1. For three representative lattices (the stretching-dominated octahedron and octet, and the bending-dominated bitruncated octahedron, also known as Kelvin foam), we show the effect of increasing the relative density in the low-density regime (ensuring slender struts with $\frac{D}{L_s} \leq 0.1$, D and L_s being the diameter and length, respectively, of the struts with circular cross-section). Note that all struts/beams in each structure have identical beam lengths, while their diameters vary with density. While all three architectures show an increase in their effective uniaxial stiffness with increasing density (by one order of magnitude for the shown density range of $1\% - 3\%$), the impact on energy absorption is distinctly different and notably non-monotonic. Against the general trend, the octahedron dissipates less impact energy with increasing density. The energy absorption, measured as the difference in the impactor's kinetic energy before and after the impact, depends on the chosen impact speed (besides impactor size and shape). The chosen impactor (a stiff disk of radius $r_i = 60$ mm and mass $m_i = 48.43$ g) generally shows increasing dissipation with increasing speed—in excellent agreement with experimental data, as shown in Fig. 1. The finite element simulations are based on corotational beam elements [35] and a linear viscoelastic constitutive model for the base material. We adopt the numerical framework of 3D linear viscoelastic slender beams of [23], which accounts for finite rotations of the beams while considering infinitesimal (linearized) axial, flexural, and torsional strains. To properly capture the viscoelastic behavior of the material used in this study, a generalized Maxwell model was calibrated experimentally for the thermoplastic base material of the 3D-printed samples by identifying the parameters of the associated Prony series from quasistatic uniaxial relaxation experiments on 3D-printed dogbone samples, following the procedure outlined in [23]. The complete Prony series parameters are provided in Table 1. The impactor was modeled as a rigid body that freely fell in a vacuum and indented the sample through an interaction potential [36], starting from rest. Simulations were performed using the open-source finite element code ae108 [37].

Table 1
Modulus values and corresponding relaxation times obtained from the calibration of the Prony series for the TPE base material.

Elastic moduli	Elastic moduli values (MPa)	Relaxation	Relaxation times (s)
E_∞	5600	-	-
E_1	7270	τ_1	0.3
E_2	791	τ_2	3.0
E_3	465	τ_3	30.0
E_4	570	τ_4	300.0

The truss lattice samples, measuring $110\,\text{mm}^3$ in outer dimensions and containing 10 x 10 x 10 unit cells, were designed based on the nodal coordinate and connectivity information and were 3D-printed on a Sintratec S1 printer via selective laser sintering with a layer thickness of 100 μm. The pre-treated elastomeric material TPE has a density of $0.95\,\text{g}\cdot\text{cm}^3$ and, when sintered, results in flexible, rubber-like parts, which can reach an elongation at a break of 430%. After printing, the residual powder was manually removed from the samples, followed by a thorough cleaning using an air-blasting cabinet. The experiments used an in-house drop tower, whose impactor is attached to a rod contained within a guiding tube and actuated by a release system to ensure a well-controlled drop (see Fig. 1). During experiments, the lower nodes of the structure in the direction of loading are constrained, and a high-speed image tracking system is used to track the position of the indenter's center, using the tracking code presented in [38]. For each lattice topology and density, three samples were 3D-printed and tested five times. The average values are reported in Fig. 1. As illustrated in Fig. 1, the tested samples confirm the accuracy of the simulation results. Fig. 1 further shows that changes to the architecture can lead to significant changes in both stiffness and damping and that the correlation of these two key properties is nontrivial but excellently predictable by structural analysis. As the probed experimental/simulated regime avoids beam contact and failure and wave dispersion does not considerably affect the impact response, dissipation stems primarily from the intrinsic viscoelasticity of the base material.

3. Spatially variant trusses

Spatial variation in the architecture of 3D truss lattices allows us to tailor the effective mechanical properties locally. For example, we consider a bitruncated octahedron lattice (Kelvin foam), whose unit cells are continuously stretched in the x-direction. The overall truss has the shape of a cuboid containing $8 \times 10 \times 10$ unit cells. The x-components of all node positions are displaced to $x_{\text{new}} = L(x_{\text{old}}/L)^{1/\gamma}$, where parameter $\gamma > 0$ defines the grading ($\gamma = 1$ representing a periodic truss without grading), and L is the side length of the overall truss. Fig. 2(a) shows a 3D-printed sample of such graded truss with $\gamma = 20$ and overall dimensions $(110\,\text{mm})^3$. Through the grading, the effective mechanical response changes continuously along the x-direction, including a decrease in the effective (vertical) stiffness E_{33} by 15% from left to right (obtained from periodic homogenization of a periodic truss with the unit cell taken from different locations within the graded truss; see Fig. 2(a)). Similarly, the energy absorbed during an impact modulates from left to right. To assess the impact response of the graded truss, a stiff, spherical impactor (mass $m = 48.43$ g, radius $r = 60$ mm) is dropped from a height of 170 mm above the truss (measuring the vertical distance of

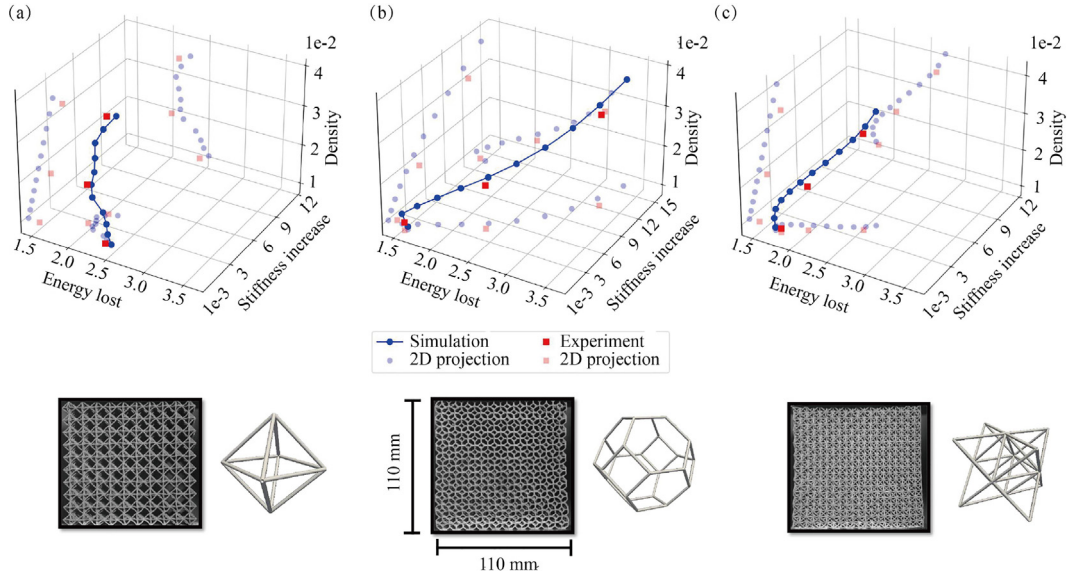

Fig. 1. Effect of the relative density of viscoelastic truss lattices (adjusted by altering the strut thickness) on the effective uniaxial stiffness E and the energy absorption J during impact for three truss topologies: (a) octahedron, (b) bitruncated octahedron (Kelvin foam), and (c) octet. The 3D property maps include the 2D projections in the three planes. Photographs and CAD unit cells illustrate the three designs.

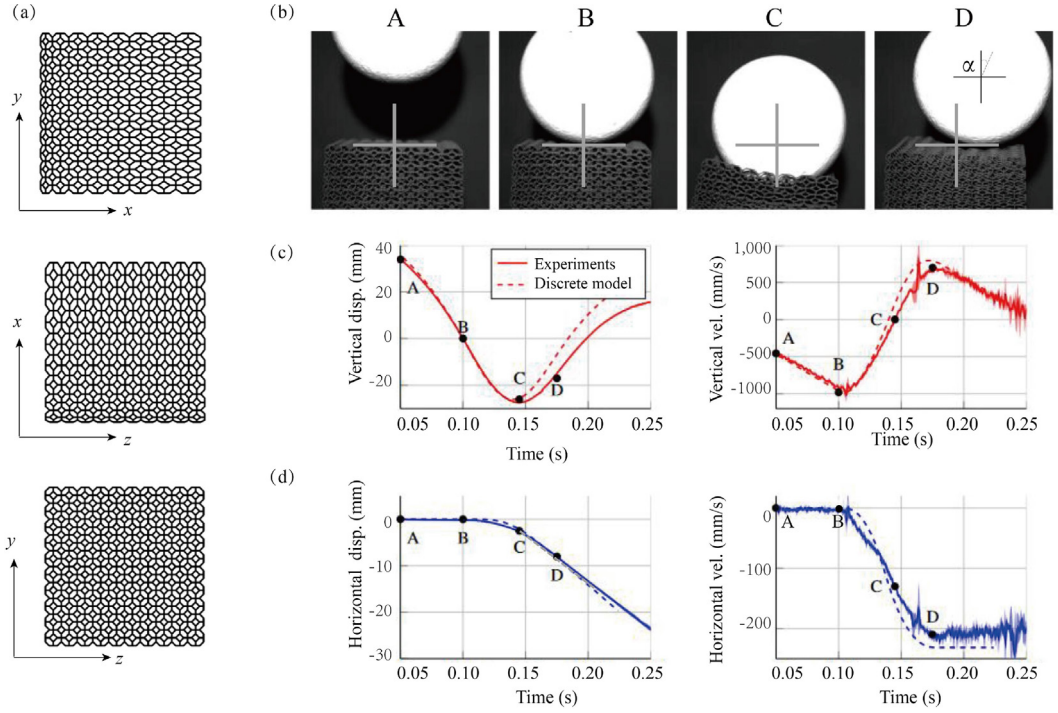

Fig. 2. Impact into a spatially graded bitruncated octahedron lattice, shown in (a) as its three surface projections. (b) Snapshots of the rigid spherical impactor: instant A shows the lattice and impactor before impact; instant B the impactor comes into contact with the lattice; instant C is the turn-around point of the impactor, and at instant D, the impactor leaves the truss (loses contact) under an angle $\alpha = 23°$ against the vertical axis. (c,d) Averaged vertical (red) and horizontal (blue) displacement and velocity measurements throughout the experiments, highlighting the four instants A through D from (b). (For interpretation of the references to colour in this figure legend, the reader is adviced to consult the web version of this article.)

the indenter's center to the sample's surface before release), reaching an average impact speed of $v_B = 1005$ mm · s at contact. A high-speed camera tracks the center point of the falling and rebounding sphere at a rate of 4000 frames per second. Measurements are averaged over ten consecutive experiments, which indicate excellently reproducible data. Fig. 2 presents the time-dependent vertical (Fig. 2(c)) and horizontal displacement (Fig. 2(d)) along with the velocity components of the impactor, which enters the truss up to point C, where it reverts its direction and finally loses contact at point D. The considerable difference between the entry and exit velocities (here of about $\Delta v = |v_B - v_D| = 1700$ mm · s^{-1}) characterizes the energy lost during impact and hence the energy absorption capability of the viscoelastic truss, as described in Section 2. Unlike there, however, the spatial grading introduces a new effect here.

The horizontal versus vertical displacement and velocity data confirm what can be observed visually during experiments: the vertically impacting sphere leaves the truss with a non-zero horizontal velocity

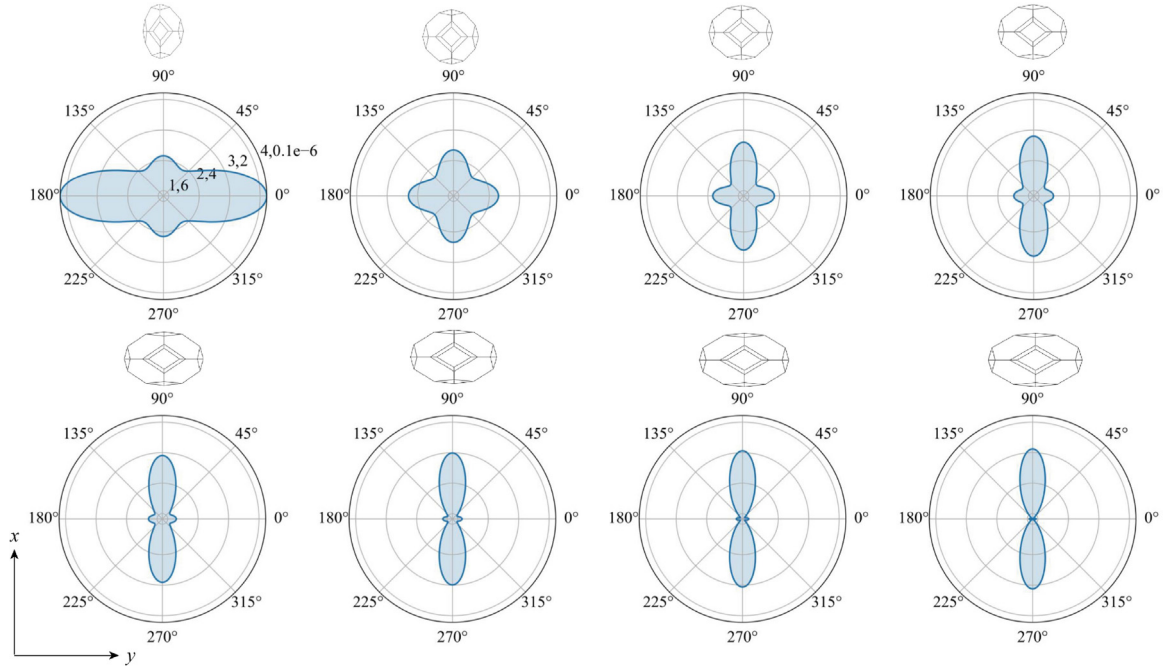

Fig. 3. Directional Young's modulus maps of the eight-unit cells in the spatially variant bitruncated octahedron sample. Each subplot represents the polar plot of the directional stiffness of a unit cell, as calculated from their respective homogenized 3D stiffness tensors (based on the periodic homogenization of each unit cell). The angle represents the direction of the applied load in the $x-y$ plane. At the same time, the radial distance indicates the stiffness value normalized by the base material's Young's modulus (the first plot includes stiffness magnitude labels for reference, which are identical for all plots but omitted for clarity).

component of approximately 200 mm · s, thus changing its initially vertical trajectory into a new direction. The observed deviation angle of $\alpha = 23°$ stems from the spatial grading of the truss and the associated stiffness reduction in the direction of the spatial grading, allowing the impactor to penetrate deeper (and over a longer in time) with increasing x-position. This is confirmed in Fig. 3, showing the directional stiffness of each of the eight unit cells in the graded sample, arranged from the smallest to the largest (from left to right, respectively). Homogenized stiffness tensors were computed by assuming an infinite periodic medium for each unit cell and performing computational homogenization with periodic boundary conditions [27,39]. The presented stiffness plots are projections of the 3D elastic modulus surface onto the $x-y$-plane, indicating the variation of the uniaxial Young's modulus with orientation in the $x-y$ plane. Aside from the strong changes in anisotropy with unit cell geometry, we observe a clear decrease in the vertical stiffness (along the y-axis) when transitioning from left to right along the x-axis. Notably, by construction, all unit cells have the same slenderness ratio. Taking the simple analogy of a stiff mass impacting an elastic 1D medium of stiffness E, density ρ and height h, the characteristic impact time until rebound is twice the travel time of the compressive impulse through the medium, $\Delta t = h/\sqrt{E/\rho}$. As h and ρ are constant throughout the graded sample, the rebound time relates inversely to the stiffness – which in our cases varies from left to right as shown in Fig. 3 (E is the shown value in the vertical direction). Consequently, the graded stiffness is responsible for the directional rebound, and the stiffness grading can be used to control the impact response.

The result is a graded penetration and hence a directional bias (showing convincing agreement between simulations and experiments, the latter yielding a slightly stiffer response). Based on the calculated coefficient of restitution, the total absorbed energy by the graded lattice ($e_{\text{graded bioct.}} = |v_D/v_B| = 0.77$) is almost identical to that of an impactor hitting a non-graded, periodic bitruncated octahedron truss ($e_{\text{bioct.}} = 0.75$), whose periodic unit cell is at the center of the graded truss. Hence, the spatial grading did not degrade the energy absorption but added a directional bias, which admits, e.g., to sort impacting particles based on their impact velocity mechanically.

To gain insight into the effect of the viscoelastic base material and the spatial grading, Fig. 4(a) shows the simulated total force vs. time response, recorded at the top and bottom surfaces of the sample during impact, for three different samples, all having bitruncated octahedral lattice topologies: a viscoelastic periodic one, a viscoelastic spatially graded one, and a linear elastic spatially graded one (having the same long-term elastic moduli as the viscoelastic sample). Snapshots of the evolving local instantaneous elastic energy distribution in the corresponding samples are illustrated in Fig. 4(b)-(d). The evaluated lattices are tested under the same impact conditions used in Section 3. The force-time plot (Fig. 4(a)) reveals the profiles of forces applied to (top) and transmitted through (bottom) both viscoelastic and elastic samples. As expected, the viscoelastic lattices attenuate force oscillations at the reactive end over time, consistent with the dissipative behavior intrinsic to viscoelastic materials, while the linear elastic lattice (Fig. 4(b)) demonstrates persistent oscillations with lower energy dissipation. The uniform force distribution in the viscoelastic homogeneous lattice (Fig. 4(d)) suggests that, while it benefits from the viscoelastic behavior in terms of damping (as the graded one), it lacks the tailored deformation pathway provided by structural grading, which in the directional rebound visible in Fig. 4(b).

Under impact loading, as observed in Fig. 4(b)-(c), the graded lattice leverages the stretching and bending deformation of its members more efficiently, allowing for a tailored response to the applied force. As discussed above, the variation in unit cell stiffness facilitates a progressive energy absorption, where the impact force initially engages the stiffer, smaller cells, gradually involving the softer, larger cells. This gradation not only enhances the energy dissipation through bending but also introduces a stretching component due to the axial forces generated in the direction of gradation. In contrast, the periodic lattice in Fig. 4(d), having a uniform unit cell size and effective stiffness throughout its structure, results in a more isotropic deformation response to impact, with energy absorption and dissipation symmetrically distributed across the lattice. In this symmetric deformation, the bending-dominated deformation mechanisms of the bitruncated octahedral lattice topology are predominant, with less opportunity for the lattice to exploit axial stretching

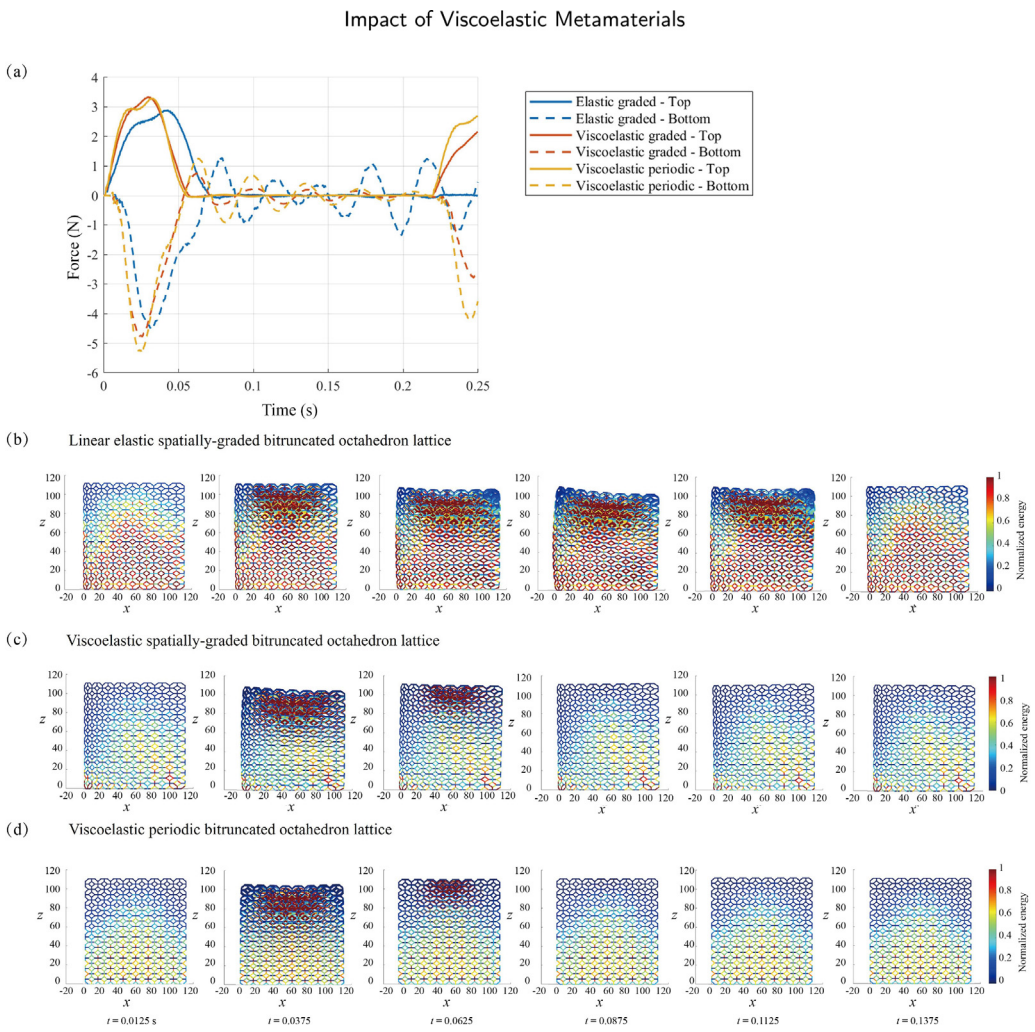

Fig. 4. (a) Comparison of the simulated forces vs. time responses for three truss samples during impact, where the top and bottom forces represent the applied net force by the indenter and the reaction force from the ground, respectively: a viscoelastic bitruncated octahedral lattice (also shown in (b)), a viscoelastic spatially graded bitruncated octahedral lattice (also shown in (c)), and, for reference, the same spatially graded bitruncated octahedral lattice with linear elastic base material properties (adopting the long-term elastic modulus of the viscoelastic base material, shown in (d)). Snapshots were taken at given time steps during and after impact; the color code illustrates the normalized local stored elastic energy in the beams of the samples.

in absorbing and dissipating the impact energy. The dual-mode deformation under impact – combining bending with stretching – affords the graded lattice slightly superior energy absorption and, especially, the directional response absorbed in our simulations and experiments. Note that the progressive engagement of lattice cells from stiff to soft may also help distribute the impact forces, mitigating potential stress concentrations and enhancing the structural integrity under load (though this requires further characterization and examination of local stress concentrations and potential failure mechanisms of the base material, which is beyond the scope of this study).

4. Spatially variant truss lattice sheets

Inspired by the popularity of 2D materials [40], this study extends the aforementioned design paradigm to viscoelastic 2D truss lattice sheets with spatial grading. Spatially variant 2D structures are generated using a design parameterization that switches between hexagonal and re-entrant honeycomb unit cells [41–43]. As shown in Fig. 5, the unit cell with two orthogonal symmetries is tailorable by four geometric parameters: the lengths a, b, L_x, and L_y (for a unit cell of dimensions $L_x \times L_y$). In this examples, the aspect ratio L_y/L_x is fixed for simplicity, leaving three design parameters. In general, the unit cell has $n_n = 8$ nodes and $n_b = 8$ beams, though for certain choices of parameters (e.g., $b = L_x$) overlapping nodes are condensed into one (and beams of zero length are removed).

Fig. 3(b) illustrates a spatially variant 2D lattice obtained from interpolating the UC parameters a and b (at fixed L_x and L_y and aspect ratio $L_y/L_x = \sqrt{3}$) from a set of control points. Specifically, we define the UC geometry at the four shown control points by (counterclockwise starting from the bottom left) $a = b = \sqrt{3}L_y/3$, $a = b = 0$, $a = L_y$ and $b = 0$, and $a = b = \sqrt{3}L_y/2$. Interpolation (as well as extrapolation) across the entire domain is achieved based on the Gaussian-type shape functions

$$\tilde{N}_i(\mathbf{X}) = \frac{N_i(\mathbf{X})}{\sum_{j=1}^{4} N_j(\mathbf{X})} \text{ with } N_i(\mathbf{X}) = \exp\left(-\beta\left|\mathbf{X} - \mathbf{X}_{\text{CP}}^{(i)}\right|^2\right), \tag{1}$$

where $\beta > 0$ defines the width of shape functions (for the example in Fig. 6 we use $\beta = 4$). For fixed L_x and L_y, we interpolate the geometric parameters a and b based on their values at the four control points and based on the shape functions in Eq. (1) evaluated at the geometric center of each unit cell within the domain. Parameter β controls the width of the transition zones between control points, providing a seamless functional grading. While $\beta = 0$ results in a non-variant, periodic mesh whose unit cell has the average value of all control point unit cells,

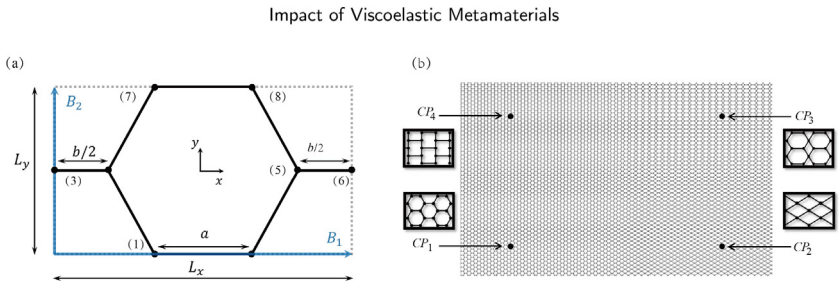

Fig. 5. Geometric description of 2D spatially-graded unit cells. (a) The UC consists of eight beams connecting the eight nodes. Parameters a, b, L_x, and L_y define the UC geometry. (b) Example of a 2D spatially variant lattice with an aspect ratio of $L_y/L_x = \sqrt{3}$, described by four different UC geometries displayed in the magnifications, and four control points. Interpolation (and extrapolation) between these four UCs allows for smooth transitions.

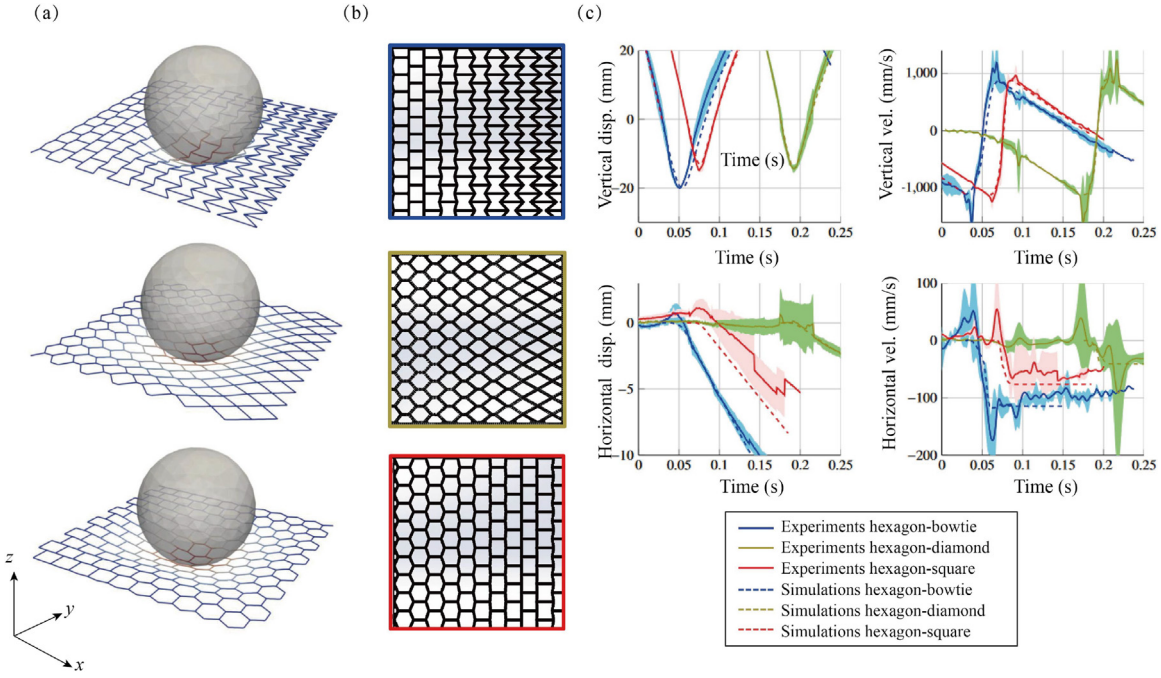

Fig. 6. Impact into a spatially graded 2D truss lattice sheet. (a) Simulated response of three spatially graded sheets (interpolating between, from top to bottom, hexagonal and bowtie, hexagonal and diamond, and hexagonal and square UCs). (b) Top view of the 3D-printed undeformed spatially variant lattices. (c) Comparison of the impactor's trajectory when rebounding from the three spatially variant truss sheets, showing its horizontal x and vertical y displacement and velocity components as obtained from simulations and from tracking the impactor's position in experiments.

the limit $\beta \to \infty$ represents a spatially-variant lattice with regions of uniform UCs separated by sharp transitions (each UC uniquely belonging to the nearest control point). Note that the choice of β depends on the distance between control points (and β may be normalized accordingly for a size-independent interpolation parameter).

Fig. 6 shows three spatially variant lattices obtained from interpolating between two UCs in each case: hexagon to bowtie, hexagon to diamond, and hexagon to square. As before, each spatially variant structure is simulated (see Fig. 6(a)) using corotational beam elements with the same viscoelastic base material model presented above. To mimic experiments, we assume that the 2D spatially variant structures (and periodic ones for references) are clamped at their outer boundary. Using the same 3D-printing procedures as before (see Fig. 6(b)), we fabricated all three spatially variant lattice sheets and tested the impact response of each sample five times, using an indenter of mass $m_i = 3.77$ g and radius $r_i = 28.5$ mm with an impact velocity of $v_i = 1505$ mm $\cdot$ s^{-1}. Horizontal and vertical displacements and velocities of the indenter over time as obtained from both experiments and simulations are compared in Fig. 6(c). Overall, simulations and experiments demonstrate convincing agreement (especially when considering the relatively simple beam and viscoelastic constitutive models used). A maximum impact depth of 20 mm is observed for the hexagon-to-bowtie lattice, while it is approximately 17.5 mm for the other two. Consequently, the (average) rebound vertical speed of the impactor is maximal for the hexagon-to-bowtie lattice with approximately $v_{\text{out}} = 1000$ mm $\cdot$ s^{-1} in simulations and $v_{\text{out}} =\sim 1024$ mm $\cdot$ s^{-1} in experiments.

The hexagon-to-bowtie and hexagon-to-square designs redirect the rebound trajectory of the impactor by approximately 23 deg from the vertical axis, compared to 3 deg for the hexagon-to-diamond case. This stark contrast can, again be explained by the effective elastic properties of the UCs. The effective elastic properties of the hexagon and diamond UCs are almost identical when stretched during impact (see Table 2), making the rebound close to vertical. Contrarily, the bowtie UC is con-

Table 2
The effective Young's modulus, Poisson's ratio, and shear modulus of four 2D unit cells, normalized by the base material's Young's Modulus E. The effective (isotropic reference) moduli are computed from the homogenized 3D compliance tensor $\mathbf{S} = \mathbb{C}^{-1}$ via $\bar{E} = \frac{1}{3}\left(\frac{1}{S_{11}} + \frac{1}{S_{22}} + \frac{1}{S_{33}}\right)$, $\bar{\nu} = \frac{1}{3}\left(\frac{S_{12}}{S_{11}} + \frac{S_{13}}{S_{11}} + \frac{S_{23}}{S_{22}}\right)$, and $\bar{G} = \frac{1}{3}\left(\frac{1}{S_{44}} + \frac{1}{S_{55}} + \frac{1}{S_{66}}\right)$. They characterize, respectively, the axial strength, Poisson effect, and the shear resistance of the structure.

	Hexagon	Bowtie	Square	Diamond
$\bar{E}/E$	7.652×10^{-3}	9.114×10^{-5}	7.854×10^{-5}	8.068×10^{-3}
$\bar{\nu}$	0.971	−0.330	0.000	0.985
$\bar{G}/E$	1.98×10^{-5}	3.434×10^{-3}	3.945×10^{-5}	2.602×10^{-3}

siderably softer than the hexagon UC when stretched during impact, which leads to a deflection of the impactor and a horizontal speed after impact of approximately 120 mm · s^{-1}. Therefore, the choice of the right combination of unit cells can be used effectively to control the rebound of the impactor. Moreover, increasing the incoming velocity of the impactor increases the indentation depth, which leads to a higher rebound angle.

5. Conclusion

We have shown how periodic and spatially graded polymer-based viscoelastic truss lattices in 2D and 3D behave during impact and how this behavior can be controlled through the geometric design of the lattice. The employed beam-based computational model is highly efficient and accurately predicts the response of various truss lattices in experiments (once calibrated [23], it predicts the response of complex 2D and 3D lattices well). We have demonstrated that periodic 3D lattices cover a wide domain in the stiffness versus energy absorption space (two important and often mutually exclusive properties of architected materials). Moreover, we have shown how spatial variations in the unit cell topology in 3D lattices and 2D lattice sheets can effectively redirect the impactor and how unit cell changes can be used to control the extent of redirection (using the homogenized elastic stiffness of a unit cell as a key metric to understand the impactor's redirection).

Our findings give insight into the structure-property relations of periodic and spatially graded viscoelastic trusses, emphasizing their potential applications in areas such as advanced protective gear, automotive safety components, and vibration damping solutions. Additionally, we demonstrate that beam-based finite element simulations can accurately and efficiently capture the mechanical response of 3D-printed truss lattices under various impact conditions. The proposed architectures offer opportunities for controlling the impact response through architected materials, enabling enhanced energy absorption (making them interesting for, e.g., protective gear or body armor) and especially for as-designed impact redirection (of interest, e.g., in sports equipment, soft robotics, or reconfigurable metamaterials). While the 3D-printed thermoplastic provided the viscoelastic properties of the base material, optimizing the 3D-printing process and post-processing could allow the viscoelastic material properties to serve as design variables

Decalaration of Competing Interest

The authors declare that they have no known competing financial interests or personal relationships that could have appeared to influence the work reported in this paper.

CRediT authorship contribution statement

Kaoutar Radi: Writing – review & editing, Writing – original draft, Visualization, Validation, Methodology, Investigation, Formal analysis, Conceptualization. **Raphaël N. Glaesener:** Writing – original draft, Methodology, Investigation. **Siddhant Kumar:** Methodology. **Dennis M. Kochmann:** Writing – review & editing, Writing – original draft, Supervision, Methodology.

References

[1] H.M. Kolken, S. Janbaz, S.M. Leeflang, K. Lietaert, H.H. Weinans, A.A. Zadpoor, Rationally designed meta-implants: a combination of auxetic and conventional meta-biomaterials, Mater. Horiz. 5 (1) (2018) 28–35.

[2] B. Telgen, Leveraging architected materials in structural systems for optimized design and control of wave motion, ETH Zurich, 2021 Ph.D. thesis.

[3] D.J.N. Amorim, T. Nachtigall, M.B. Alonso, Exploring mechanical meta-material structures through personalised shoe sole design, in: Proceedings of the ACM Symposium on Computational Fabrication, 2019, pp. 1–8.

[4] C. Laschi, M. Cianchetti, Soft robotics: new perspectives for robot bodyware and control, Front. Bioeng. Biotechnol. 2 (2014) 3.

[5] J.N. Grima, D. Attard, R. Gatt, Truss-type systems exhibiting negative compressibility, Phys. Status Solidi (B) Basic Res. 245 (11) (2008) 2405–2414, doi:10.1002/pssb.200880267.

[6] K. Bertoldi, P.M. Reis, S. Willshaw, T. Mullin, Negative poisson's ratio behavior induced by an elastic instability, Adv. Mater. 22 (3) (2010) 361–366.

[7] Y. Tsuda, O. Mori, R. Funase, H. Sawada, T. Yamamoto, T. Saiki, T. Endo, J. Kawaguchi, Flight status of IKAROS deep space solar sail demonstrator, Acta Astronaut. 69 (9–10) (2011) 833–840, doi:10.1016/j.actaastro.2011.06.005.

[8] S.A. Zirbel, R.J. Lang, M.W. Thomson, D.A. Sigel, P.E. Walkemeyer, B.P. Trease, S.P. Magleby, L.L. Howell, Accommodating thickness in origami-based deployable arrays1, J. Mech. Des. Trans. ASME 135 (11) (2013) 1–11, doi:10.1115/1.4025372.

[9] J.R. Raney, N. Nadkarni, C. Daraio, D.M. Kochmann, J.A. Lewis, K. Bertoldi, Stable propagation of mechanical signals in soft media using stored elastic energy, Proc. Natl. Acad. Sci. 113 (35) (2016) 9722–9727.

[10] A. Ion, J. Frohnhofen, L. Wall, R. Kovacs, M. Alistar, J. Lindsay, P. Lopes, H.-T. Chen, P. Baudisch, Metamaterial mechanisms, in: Proceedings of the 29th annual symposium on user interface software and technology, 2016, pp. 529–539.

[11] B.F. Haynes, W. Chen, Y. Feng, D.S. Dimitrov, G. Kelsoe, S.C. Harrison, T.B. Kepler, N.S. Longo, D.E. Russ, H.W. Sun, P.E. Lipsky, S. Kupriyanov, A 3D-printed, functionally graded soft robot powered by combustion 349 (6244) (2015) 161–165.

[12] A.J. Zelhofer, D.M. Kochmann, On acoustic wave beaming in two-dimensional structural lattices, Int. J. Solids Struct. 115 (2017) 248–269.

[13] M. Mohsenizadeh, F. Gasbarri, M. Munther, A. Beheshti, K. Davami, Additively-manufactured lightweight metamaterials for energy absorption, Mater. Des. 139 (2018) 521–530, doi:10.1016/j.matdes.2017.11.037.

[14] Z. Ozdemir, E. Hernandez-Nava, A. Tyas, J.A. Warren, S.D. Fay, R. Goodall, I. Todd, H. Askes, Energy absorption in lattice structures in dynamics: experiments, Int. J. Impact Eng. 89 (2016) 49–61, doi:10.1016/j.ijimpeng.2015.10.007.

[15] M. Gomez, D.E. Moulton, D. Vella, Dynamics of viscoelastic snap-through, J. Mech. Phys. Solids 124 (2019) 781–813.

[16] D.M. Dykstra, J. Busink, B. Ennis, C. Coulais, Viscoelastic snapping metamaterials, J. Appl. Mech. 86 (11) (2019).

[17] S. Janbaz, K. Narooei, T. van Manen, A. Zadpoor, Strain rate–dependent mechanical metamaterials, Sci. Adv. 6 (25) (2020) eaba0616.

[18] Y. Wang, S. Arabnejad, M. Tanzer, D. Pasini, Hip implant design with three-dimensional porous architecture of optimized graded density, J. Mech. Des. 140 (11) (2018).

[19] R.F. Ghachi, W.I. Alnahhal, O. Abdeljaber, J. Renno, A.B.M. Tahidul Haque, J. Shim, A. Aref, Optimization of viscoelastic metamaterials for vibration attenuation properties, Int. J. Appl. Mech. 12 (10) (2020) 2050116, doi:10.1142/S1758825120501161.

[20] W.J. Parnell, R. De Pascalis, Soft metamaterials with dynamic viscoelastic functionality tuned by pre-deformation, Philos. Trans. R. Soc. A 377 (2144) (2019) 20180072.

[21] Y. Liu, T.A. Schaedler, X. Chen, Dynamic energy absorption characteristics of hollow microlattice structures, Mech. Mater. 77 (2014) 1–13, doi:10.1016/j.mechmat.2014.06.008.

[22] C.M. Portela, B.W. Edwards, D. Veysset, Y. Sun, K.A. Nelson, D.M. Kochmann, J.R. Greer, Supersonic impact resilience of nanoarchitected carbon, Nat. Mater. (2021) 1–7.

[23] R.N. Glaesener, J.H. Bastek, F. Gonon, V. Kannan, B. Telgen, B. Spöttling, S. Steiner, D.M. Kochmann, Viscoelastic truss metamaterials as time-dependent generalized continua, J. Mech. Phys. Solids 156 (June) (2021) 104569, doi:10.1016/j.jmps.2021.104569.

[24] R. Lakes, Viscoelastic Solids, CRC Mechanical Engineering Series, CRC Press, 1999.

[25] L.R. Meza, S. Das, J.R. Greer, Strong, lightweight, and recoverable three-dimensional ceramic nanolattices, Science 345 (6202) (2014) 1322–1326, doi:10.1126/science.1255908.

[26] C.M. Portela, A. Vidyasagar, S. Krödel, T. Weissenbach, D.W. Yee, J.R. Greer, D.M. Kochmann, Extreme mechanical resilience of self-assembled nanolabyrinthine materials, Proc. Natl. Acad. Sci. U.S.A. 117 (11) (2020) 5686–5693, doi:10.1073/pnas.1916817117.

[27] R.N. Glaesener, C. Lestringant, B. Telgen, D.M. Kochmann, Continuum models for stretching-and bending-dominated periodic trusses undergoing finite deformations, Int. J. Solids Struct. 171 (2019) 117–134.

[28] G.P. Phlipot, D.M. Kochmann, A quasicontinuum theory for the nonlinear mechanical response of general periodic truss lattices, J. Mech. Phys. Solids 124 (2019) 758–780.

[29] T.A. Schaedler, A.J. Jacobsen, A. Torrents, A.E. Sorensen, J. Lian, J.R. Greer, L. Valdevit, W.B. Carter, Ultralight metallic microlattices, Science 334 (6058) (2011) 962–965.

[30] L. Meza, J. Greer, Mechanical characterization of hollow ceramic nanolattices, J. Mater. Sci. 49 (6) (2014) 2496–2508.

[31] L.R. Meza, G.P. Phlipot, C.M. Portela, A. Maggi, L.C. Montemayor, A. Comella, D.M. Kochmann, J.R. Greer, Reexamining the mechanical property space of three--dimensional lattice architectures, Acta Mater. 140 (2017) 424–432.

[32] V.S. Deshpande, N.A. Fleck, M.F. Ashby, Effective properties of the octet-truss lattice material, J. Mech. Phys. Solids 49 (8) (2001) 1747–1769.

[33] V. Deshpande, M. Ashby, N. Fleck, Foam topology: bending versus stretching dominated architectures, Acta Mater. 49 (6) (2001) 1035–1040.

[34] C.M. Portela, J.R. Greer, D.M. Kochmann, Impact of node geometry on the effective stiffness of non-slender three-dimensional truss lattice architectures, Extreme Mech. Lett. 22 (2018) 138–148.

[35] M.A. Crisfield, Non-linear Finite Element Analysis of Solids and Structures – Vol. 1, John Wiley & Sons Ltd., Chichester, England, 1991.

[36] C.L. Kelchner, S.J. Plimpton, J.C. Hamilton, Dislocation nucleation and defect structure during surface indentation, Phys. Rev. B 58 (1998) 11085–11088.

[37] Mechanics, M. Lab, ae108, 2020, 10.5905/ethz-1007-257.

[38] K. Radi, F. Allamand, D.M. Kochmann, Deformation tracking of truss lattices under dynamic loading based on Digital Image correlation, Mech. Mater. 183 (May) (2023) 104658, doi:10.1016/j.mechmat.2023.104658.

[39] R.N. Glaesener, E.A. Träff, B. Telgen, R.M. Canonica, D.M. Kochmann, Continuum representation of nonlinear three-dimensional periodic truss networks by on-the-fly homogenization, Int. J. Solids Struct. 206 (2020) 101–113.
[40] C. Reddy, S. Rajendran, K. Liew, Equivalent continuum modeling of graphene sheets, Int. J. Nanosci. 4 (04) (2005) 631–636.
[41] T. Mukhopadhyay, S. Adhikari, Stochastic mechanics of metamaterials, Compos. Struct. 162 (2017) 85–97, doi:10.1016/j.compstruct.2016.11.080. http://www.sciencedirect.com/science/article/pii/S0263822316321171.
[42] M. Mirzaali, A. Caracciolo, H. Pahlavani, S. Janbaz, L. Vergani, A. Zadpoor, Multi–material 3d printed mechanical metamaterials: rational design of elastic properties through spatial distribution of hard and soft phases, Appl. Phys. Lett. 113 (24) (2018) 241903.
[43] M. Mirzaali, S. Janbaz, M. Strano, L. Vergani, A.A. Zadpoor, Shape-matching soft mechanical metamaterials, Sci. Rep. 8 (1) (2018) 1–7.